



Article

A Rotor Position Detection Method for Permanent Magnet Synchronous Motors Based on Variable Gain Discrete Sliding Mode Observer

Mingchen Luan, Yun Zhang , Xiaowei Li and Fenghui Xu

School of Rail Transportation, Shandong Jiaotong University, Jinan 250357, China;
22121003@stu.sdjtu.edu.cn (M.L.); lixiaowei@sdjtu.edu.cn (X.L.); xufh@tellhow.com (F.X.)

* Correspondence: zhangyun@sdjtu.edu.cn

Abstract: The purpose of this paper is to study the sensor-less rotor position estimation method for permanent magnet synchronous motors, and to achieve accurate estimation of rotor position in different conditions. Firstly, the traditional super-twisting observer algorithm is analyzed, and a new discrete variable gain sliding mode observer is designed to solve the buffeting problem in discrete systems, taking the reaction force as the disturbance signal. By estimating the back potential of the observer, the buffeting problem in the sliding mode algorithm can be effectively improved as shown by the simulation results. Then, to solve the problem of phase delay in rotor position estimation, an adaptive orthogonal phase-locked loop method is used to compensate the estimation error caused by the change in motor speed and increase the estimation accuracy of rotor position. The stability of the method can be proven by Lyapunov's second method. Simulation experiments verify the accuracy of the proposed PMSM rotor position estimation method.

Keywords: permanent magnet synchronous motor; rotor position estimation; adaptive quadrature phase-locked loop; discrete variable gain sliding mode observer



Citation: Luan, M.; Zhang, Y.; Li, X.; Xu, F. A Rotor Position Detection Method for Permanent Magnet Synchronous Motors Based on Variable Gain Discrete Sliding Mode Observer. *World Electr. Veh. J.* **2024**, *15*, 87. <https://doi.org/10.3390/wevj15030087>

Academic Editors: Xinmin Li, Liyan Guo and Joeri Van Mierlo

Received: 10 January 2024

Revised: 14 February 2024

Accepted: 22 February 2024

Published: 27 February 2024



Copyright: © 2024 by the authors. Licensee MDPI, Basel, Switzerland. This article is an open access article distributed under the terms and conditions of the Creative Commons Attribution (CC BY) license (<https://creativecommons.org/licenses/by/4.0/>).

1. Introduction

In recent decades, permanent magnet synchronous machines (PMSMs) have been extensively applied in various drive fields ranging from servo drives, robotics, electric vehicles to aerospace engineering owing to their superior characteristics, such as high efficiency, high power density, high torque-to-volume ratio, wide speed range, and reliable operations [1]. As the essential information in the high-performance field-oriented control (FOC) system, the accurate rotor position is often obtained from the shaft-mounted mechanical encoders, which, in turn, may result in a reduction in robustness, additional volume and limited applications in high-frequency vibration and humidity, and high-temperature environments. Therefore, PMSMs with position sensor-less control have attracted more and more attention [2].

The sliding mode observer method has the advantages of being simple, robust, rapid convergence, and easy to implement. PMSM sensor-less control systems rely heavily on it [3]. Initially, the traditional sliding mode observer requires the establishment of a mathematical model and the subsequent design of the sliding mode surface and control law based on the controlled object [4]. Position-free control of permanent magnet synchronous motors necessitates the design of a sliding mode observer for the stator current using the sliding mode algorithm [5]. The sliding mode equivalent control principle is used to estimate back potential and interference signals are eliminated using filtering techniques. Inverse tangent calculations, phase-locked loop methods, and other approaches can all be used to obtain rotor position estimation [6].

The basic sliding mode observer's control law has a symbol function that causes high-frequency chattering. To eliminate interference signals, a filter must be employed. The

use of a filter results in an increase in computational load and a reduction in the dynamic response capability of the system, which can cause phase delay. To obtain back potential and reduce phase delay amplitude after signal processing, an adaptive filter is proposed in reference [7]. The chattering phenomenon observed in the observed results is mitigated by replacing the switching function with a sigmoid function in Reference [8]. The chattering phenomenon in sliding mode algorithms can be improved by incorporating a sign function into the integral term in higher-order sliding mode arithmetic. The superhelix algorithm is used in References [9–12] to estimate back potential values and reduce observation errors by designing variable sliding mode gain. The State-of-Health (SOH) of alternating DC-DC boost conversion systems is estimated in the literature [13] through data-based methods, which alleviate issues like system mismatch aging and enhance overall system lifespan. We have gained inspiration by analyzing and verifying the research presented in these papers. Although there have been recent improvements in position sensor-less control theory for permanent magnet synchronous motors, challenges such as chattering and phase delay during rotor position observations still need further investigation and resolution [14–18].

The purpose of this paper is to propose a method for observing permanent magnet synchronous motors that does not care about position, using discrete systems and the super spiral sliding mode. As a summary, the main contributions of this study can be summarized as follows:

- (1) The problem of rotor position estimation buffeting in sliding mode observers is addressed by proposing a novel observer control law based on the supersonic sliding mode. By using this method, the gain can be adjusted in real-time depending on the rotor speed, which ensures that the error between the actual value and estimated value stays within a small range.
- (2) An adaptive phase-locked loop (PLL) approach is used to account for phase delay and other challenges when estimating rotor position. The PLL gain is adjusted adaptively based on the operating state of the rotor, thereby improving issues such as slow fixed bandwidth response during speed switching in high-speed permanent magnet synchronous motors.
- (3) The proposed position-independent observation method is demonstrated by numerical simulation results to effectively reduce buffeting and enhance corresponding speed during speed switching. Validating the system's stability under load conditions involves subjecting it to different loads at different times.

The rest of this article is arranged in the following manner: Section 2 presents the mathematical model of discrete systems for permanent magnet synchronous motors. The new discrete sliding mode observer's design methodology is explained in Section 3. The design approach for adaptive phase-locked loops is outlined in Section 4. Our proposed method is verified and validated through the use of MATLAB/Simulink 2022b simulations in Section 5. Finally, Section 6 provides a summary of this thesis.

2. Mathematical Model of a Permanent Magnet Synchronous Motor

To simplify the mathematical model of the PMSM, the motor voltage equation assumes a sinusoidal distribution of the air-gap magnetic field in the α - β axis system while neglecting eddy current and hysteresis losses [19].

$$\mathbf{u} = \begin{bmatrix} R_s + \frac{dL_d}{dt} & \omega_e(L_d - L_q) \\ -\omega_e(L_d - L_q) & R_s + \frac{dL_q}{dt} \end{bmatrix} \mathbf{i} + \mathbf{e} \quad (1)$$

where $\mathbf{u} = [u_\alpha \ u_\beta]^T$ is the stator voltage α - β -axis component; L_d and L_q are the stator inductance d-q-axis components; R_s is the stator resistance; ω_e is the electrical angular

velocity; $i = [i_\alpha \ i_\beta]^T$ is the stator current α - β -axis component, and e is the expanding counter-potential in the α - β -axis system with the expression:

$$e = \begin{bmatrix} e_\alpha \\ e_\beta \end{bmatrix} = \begin{bmatrix} -\omega_e \psi_f \sin \theta_e \\ \omega_e \psi_f \cos \theta_e \end{bmatrix} \quad (2)$$

where Ψ_f is the permanent magnet chain; θ_e is the electrical angle.

For a table-posted permanent magnet synchronous motor, the stator inductance is approximated by $L_d = L_q = L_s$. This simplifies and rewrites Equation (1) as the current equation of state.

$$\frac{di}{dt} = -\frac{R_s}{L_s}i + \frac{1}{L_s}u - \frac{1}{L_s}e \quad (3)$$

3. Design of a Sliding Mode Observer for Gain of a Discrete Variable

3.1. Design of a Conventional Super-Twisting Sliding Mode Observer

The Super-Twisting Algorithm–Sliding Mode Observer (STA-SMO) was designed by utilizing a twisting algorithm–sliding mode approach [20], which incorporates nonlinear feedback into the state variables, thereby enabling the system to achieve fast and smooth tracking and control. This algorithm offers high precision and robustness, effectively addressing the buffeting issue encountered in traditional sliding mode control.

The main reason for the chattering of the sliding mode observer is the discontinuity of the control signal, so reducing the chattering allows the signal to become continuous and smooth and have a higher derivative property. Therefore, in order to solve the problem of $\text{sign}()$ signal discontinuity at zero time, homogeneous function and integral control are added to the design of traditional super-twisting observers. For example, multiplying a homogeneous function with an absolute value before the $\text{sign}()$ function gives us the following equation:

$$\lim_{x \rightarrow 0^-} |x|^\alpha \text{sign}(x) = \lim_{x \rightarrow 0^+} |x|^\alpha \text{sign}(x) = 0, \alpha > 0 \quad (4)$$

Another way to solve the chattering problem is to introduce integrals. k_p and k_i can be designed as follows according to the first-order system model:

$$k_p = k_1 / |x_1 - \hat{x}_1|^{1/2} \quad (5)$$

$$k_i = k_2 / |x_1 - \hat{x}_1| \quad (6)$$

Therefore, the expression of the super-twisting sliding mode is as follows:

$$\begin{cases} \frac{d\hat{x}_1}{dt} = \frac{k_1}{\sqrt{|x_1 - \hat{x}_1|}} |x_1 - \hat{x}_1| \text{sign}(x_1 - \hat{x}_1) + \hat{x}_2 + p_1 \\ \frac{d\hat{x}_2}{dt} = \frac{k_2}{|x_1 - \hat{x}_1|} |x_1 - \hat{x}_1| \text{sign}(x_1 - \hat{x}_1) + p_2 \end{cases} \quad (7)$$

When the perturbation is ignored, it can be regarded as a linear PI controller with variable gain, whose gain k_p and k_i change with the absolute value of the state. We can simplify Equation (7) to Equation (8):

$$\begin{cases} \frac{d\hat{x}_1}{dt} = k_1 |x_1 - \hat{x}_1|^{\frac{1}{2}} \text{sign}(x_1 - \hat{x}_1) + \hat{x}_2 + p_1 \\ \frac{d\hat{x}_2}{dt} = k_2 \text{sign}(x_1 - \hat{x}_1) + p_2 \end{cases} \quad (8)$$

where x_1, x_2 are the state variables; \hat{x}_1, \hat{x}_2 is the estimated value of the state variables; k_1, k_2 are the sliding mode gains; p_1, p_2 are the perturbation terms.

For any constant ζ greater than zero, the following two equations must hold:

$$|p_1| \leq \zeta |x_1|^{\frac{1}{2}}; p_2 = 0 \quad (9)$$

$$k_1 > 2\zeta; k_2 > k_1 \frac{5\zeta k_1 + 4\zeta^2}{2(k_1 - 2\zeta)} \quad (10)$$

According to the literature [21], the perturbations p_1 and p_2 in Equation (8) will converge the system to the slip mode surface in finite time if the conditions of Equation (9) are met and the gains k_1 and k_2 satisfy the conditions of Equation (10).

From Equation (3), the estimated equation for the current in the α - β axis system is given as follows:

$$\frac{d\hat{\mathbf{i}}}{dt} = -\frac{R_s}{L_s}\hat{\mathbf{i}} + \frac{1}{L_s}\mathbf{u} - \frac{1}{L_s}\hat{\mathbf{e}} \quad (11)$$

where $\hat{\mathbf{i}}$ is the observed current in the α - β axis system and $\hat{\mathbf{e}}$ is the observed counter-potential.

The current error equation is obtained by subtracting Equation (3) from Equation (11).

$$\frac{d\tilde{\mathbf{i}}}{dt} = -\frac{R_s}{L_s}\tilde{\mathbf{i}} - \frac{1}{L_s}(\hat{\mathbf{e}} - \mathbf{e}) \quad (12)$$

where $\tilde{\mathbf{i}} = \hat{\mathbf{i}} - \mathbf{i}$ is the observed error value of the stator current.

When the current observation error converges and $\tilde{\mathbf{i}} = 0$, the observed value of the anti-potential equals the actual value. The estimated value of the anti-potential, designed based on the super-twisting algorithm, is:

$$\hat{\mathbf{e}} = k_1 |\tilde{\mathbf{i}}|^{\frac{1}{2}} \text{sign}(\tilde{\mathbf{i}}) - \int k_2 \text{sign}(\tilde{\mathbf{i}}) dt \quad (13)$$

The initial term of Equation (13) will gradually decrease as the current error converges. By comparing Equations (8) and (11), we can obtain the current estimation equation as follows:

$$\frac{d\hat{\mathbf{i}}}{dt} = -\frac{k_1}{L_s} |\tilde{\mathbf{i}}|^{\frac{1}{2}} \text{sign}(\tilde{\mathbf{i}}) - \int \frac{k_2}{L_s} \text{sign}(\tilde{\mathbf{i}}) dt - \frac{R_s}{L_s}\hat{\mathbf{i}} + \frac{1}{L_s}\mathbf{u} \quad (14)$$

The current error equation can be obtained by subtracting Equation (3) from Equation (14).

$$\frac{d\tilde{\mathbf{i}}}{dt} = -\frac{k_1}{L_s} |\tilde{\mathbf{i}}|^{\frac{1}{2}} \text{sign}(\tilde{\mathbf{i}}) - \int \frac{k_2}{L_s} \text{sign}(\tilde{\mathbf{i}}) dt - \frac{R_s}{L_s}\tilde{\mathbf{i}} + \frac{1}{L_s}\mathbf{e} \quad (15)$$

When the system achieves stability, the estimation error is on the sliding mode surface. This indicates that the estimated value is close to the actual value, and the rotor position can then be estimated using Equation (15). Due to the discontinuity of the sign function in practical applications, the estimated current switches back and forth on the sliding mode surface, resulting in a noticeable jittering phenomenon. In this paper, we propose a discrete variable gain super-twisting sliding mode observer that can adjust the convergence function based on the rotational speed.

3.2. Design of a Sliding Mode Observer for Discrete Variable Gain

In computerized control systems, continuous systems need to be discretized. According to the article [22], Equation (3) is discretized and expressed by Equation (16):

$$\mathbf{i}(k+1) = \left(1 - \frac{T_s R_s}{L_s}\right)\mathbf{i}(k) + \frac{T_s}{L_s}[\mathbf{u}(k) - \mathbf{e}(k)] \quad (16)$$

where k is the sampling moment; $\mathbf{i}(k)$, $\mathbf{u}(k)$, and $\mathbf{e}(k)$ are the current, voltage, and anti-potential values at moment k , respectively; and T_s is the discrete system sampling period.

To obtain anti-potential estimates, a sliding mode observer with perturbation observation compensation is designed. The current state Equation (16) is revised to remove anti-potential information.

$$\hat{\mathbf{i}}(k+1) = \left(1 - \frac{T_s R_s}{L_s}\right)\hat{\mathbf{i}}(k) + \frac{T_s}{L_s}\mathbf{u}(k) - \delta(k) \quad (17)$$

where \hat{i} is the observed value of the stator current, δ is a parameter containing an estimate of the counter potential, and $\delta(k)$ is defined as follows:

$$\delta(k) = v(k) - k_1(k) \sqrt{|\tilde{i}(k)|} \text{sat}(\tilde{i}(k)) \quad (18)$$

$$v(k+1) = K_v v(k) - T_s k_2(k) \text{sat}(\tilde{i}(k)) \quad (19)$$

where \tilde{i} is the stator current observation error and its expression is as follows:

$$\tilde{i}(k) = i(k) - \hat{i}(k) \quad (20)$$

The constant K_v is a fixed value that always satisfies $0 < K_v < 1$. The auxiliary gain, $v(k)$, is used in conjunction with the $\text{sat}(s)$ function, which is defined as follows:

$$\text{sat}(s) = \begin{cases} 1 & s \geq \frac{1}{c} \\ \arctan\left(\frac{qs}{c}\right) & |s| < \frac{1}{c} \\ -1 & s \leq -\frac{1}{c} \end{cases} \quad (21)$$

where $q = \tan(1) = 1.557$, c is the sliding mode boundary and s is the sliding mode surface. $k_1(k)$, $k_2(k)$ functions are defined as follows:

$$k_1(k) = K_{\eta 1} \sqrt{f_\sigma(k)} \quad (22)$$

$$k_2(k) = K_{\eta 2} f_\sigma(k) \quad (23)$$

$K_{\eta 1}$ and $K_{\eta 2}$ are constants. The function $f_\sigma(k)$ is bounded and defined as follows:

$$f_\sigma(k) = \begin{cases} \sigma_{\min} & 0 \leq \sigma(k) < \sigma_{\min} \\ \sigma(k) & \sigma_{\min} \leq \sigma(k) < \sigma_{\max} \\ \sigma_{\max} & \sigma(k) > \sigma_{\max} \end{cases} \quad (24)$$

where σ_{\min} , σ_{\max} , $\sigma(k)$ are defined as follows.

$$\sigma_{\max} = \frac{T_s}{L_s} \lambda_{pm} \omega_{\max} \quad (25)$$

$$\sigma_{\min} = \frac{T_s}{L_s} \lambda_{pm} \omega_{\min} \quad (26)$$

$$\sigma(k) = (1 - K_f) |x_f(k)| \quad (27)$$

where λ_{pm} is the permanent magnet magnetic chain, ω_{\max} and ω_{\min} are the maximum and minimum electrical angular velocities during motor operation [23], x_f is the low-pass filter state parameter; K_f is the low-pass filter gain, and the expression is as follows:

$$K_f = e^{-\omega_f T_s} \quad (28)$$

where ω_f is the filter cutoff frequency.

Then, the filter dynamic equation is:

$$x_f(k+1) = K_f x_f(k) + f_v(k) \quad (29)$$

where $f_v(k)$ is defined as follows:

$$f_v(k) = \begin{cases} \|v(k)\| & 0 < \|v(k)\| < v_{\max} \\ v_{\max} & \|v(k)\| > v_{\max} \end{cases} \quad (30)$$

where $v_{\max} = \sigma_{\max}$.

In summary, Figure 1 shows the structure of the new discrete variable gain sliding mode observer.

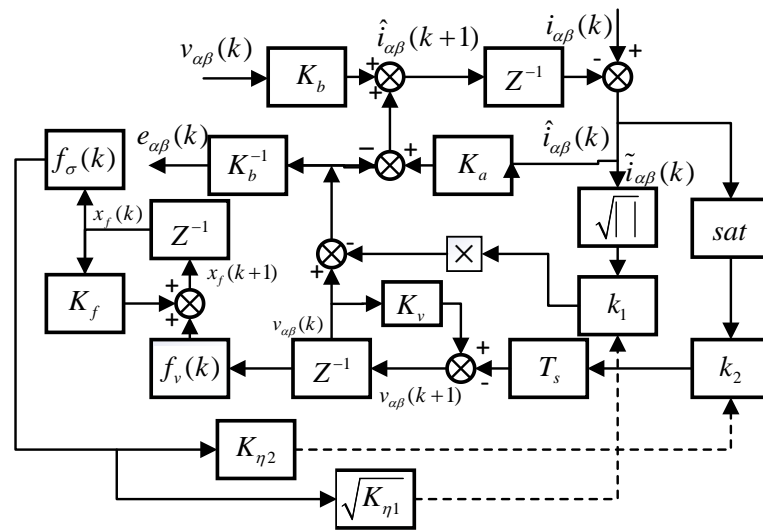


Figure 1. Structure of discrete variable gain sliding mode.

3.3. Feasibility and Convergence Analysis

3.3.1. Proof of Feasibility

The feasibility of Equation (18) is analyzed and proved as follows:

From Equation (20):

$$\tilde{\mathbf{i}}(k+1) = \mathbf{i}(k+1) - \hat{\mathbf{i}}(k+1) \tag{31}$$

By substituting Equations (16) and (17) into Equation (31), the following is obtained:

$$\tilde{\mathbf{i}}(k+1) = K_a \tilde{\mathbf{i}}(k) - K_b \mathbf{e}(k) + \delta(k) \tag{32}$$

where $K_a = 1 - \frac{T_s R_s}{L_s}$, $K_b = \frac{T_s}{L_s}$.

We can assume the existence of an ideal sliding mold surface that satisfies Equation (33).

$$\tilde{\mathbf{i}}(k+1) = \tilde{\mathbf{i}}(k) = 0 \tag{33}$$

Substituting Equation (33) into Equation (31) gives the following:

$$\delta(k) = K_b \mathbf{e}(k) \tag{34}$$

Assuming the existence of an ideal slip mold surface, Equation (18) can be rewritten as follows:

$$\delta(k) = \mathbf{v}(k) \tag{35}$$

It is possible to request the following:

$$\mathbf{v}(k) = K_b \mathbf{e}(k) \tag{36}$$

The $e(k)$ counter-potential is proportional to the rotor speed, and therefore, $v(k)$ is also proportional to the rotor speed. As $f_v(k)$ is a function of $v(k)$, it can be concluded that $f_v(k)$ is also proportional to the rotor rotational speed. This allows for the rotor rotational speed to be used in $f_v(k)$ to calculate the gain coefficients, $k_1(k)$ and $k_2(k)$, of the discrete sliding mode observer Equation (18) in real-time, achieving discrete variable gain sliding mode observation of the counter-potential.

The counter-potential can be estimated directly from Equation (34).

$$\hat{e}(k) \approx K_b^{-1} \delta(k) \quad (37)$$

Equations (18) and (32) provide the necessary information.

$$\tilde{i}(k+1) = K_a \tilde{i}(k) - K_b e(k) + v(k) - k_1(k) \sqrt{|\tilde{i}(k)|} \text{sat}(\tilde{i}(k)) \quad (38)$$

The equation above describes the updated law of the sliding mode controller in discrete time. Control input is calculated based on the current state of the sliding mode, and the sliding mode surface is updated accordingly to achieve system control through continuous iterative calculation. Equation (38) shows that K_a controls the update rate of the sliding mode surface, while K_b controls the error decay rate.

The analysis above demonstrates that the switching function trajectories described in Equations (12) and (31) always converge to the quasi-smooth mode surface of $|\tilde{i}(k)| \leq \varepsilon$, provided that the perturbation $K_b e(k)$ is bounded and there exists a value of $0 < K_a < 1$ such that $k_1(k)$, $k_2(k)$, and K_v satisfy $0 < k_1(k) \leq K_{\eta 1} (\sigma_{max})^{1/2}$, $0 < k_2(k) \leq K_{\eta 2} \sigma_{max}$, and $0 < K_v < 1$, respectively.

3.3.2. Proof of Convergence

The feasibility of the new discrete variable gain super-twisting sliding mode observer has been demonstrated through the above analysis. Next, its convergence is analyzed using the inverse method. It is assumed that the trajectory of the switching function deviates from the sliding surface, which is obtained by subtracting $\tilde{i}(k)$ on both sides of Equation (38), respectively.

$$\tilde{i}(k+1) - \tilde{i}(k) = -(1 - K_a) \tilde{i}(k) - K_b e(k) + v(k) - k_1(k) \sqrt{|\tilde{i}(k)|} \text{sat}(\tilde{i}(k)) \quad (39)$$

Assuming that $\tilde{i}(k) \rightarrow +\infty$, $\forall \tilde{i}(k) > 0$, we obtain the following:

$$\tilde{i}(k+1) - \tilde{i}(k) > 0 \quad (40)$$

By substituting Equation (40) into Equation (39), we obtain:

$$v(k) - K_b e(k) > (1 - K_a) \tilde{i}(k) + k_1(k) \sqrt{|\tilde{i}(k)|} \text{sat}(\tilde{i}(k)) \quad (41)$$

If $\tilde{i}(k) \rightarrow +\infty$, it can be seen that $v(k) \rightarrow -\infty$. Equation (42) is satisfied when $k \geq N$ such that $\tilde{i}(k+1) - \tilde{i}(k) < 0$, and the convergence condition is met.

$$v(k) - K_b e(k) < (1 - K_a) \tilde{i}(k) + k_1(k) \sqrt{|\tilde{i}(k)|} \text{sat}(\tilde{i}(k)) \quad (42)$$

Therefore, the above assumption that the trajectory of the switching function deviates from the sliding surface does not hold, showing that when $\tilde{i}(k) \rightarrow +\infty$, $\forall \tilde{i}(k) < 0$. Similarly, it can be shown that when $\tilde{i}(k) \rightarrow -\infty$, $\forall \tilde{i}(k) < 0$ does not hold. In other words, when $k \rightarrow \infty$, the trajectory of the switching function does not deviate from the sliding surface, and when the stator current error tends to 0, $v(k) \approx K_b e(k)$.

From Equation (33) and Equation (34), the conditions for the motion of the switching function on the surface of the sliding mold are as follows:

$$v(k) = K_b e(k) \Rightarrow v(k+1) = K_b e(k+1) \Leftrightarrow e(k+1) = K_v e(k) \quad (43)$$

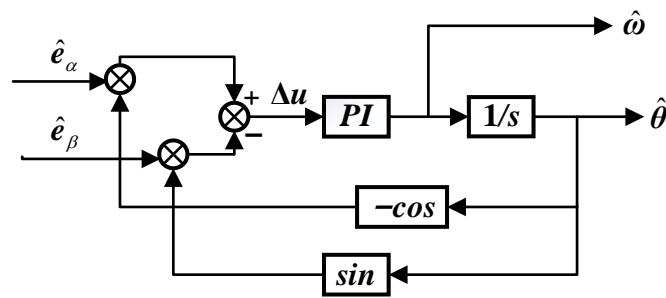


Figure 3. Structure of the phase-locked loop in the α - β axis system.

For $\hat{\omega}, \hat{\theta}$ is the estimated value of the motor rotor position and Δu is expressed as follows:

$$\Delta u = -\hat{e}_\alpha \cos \theta - \hat{e}_\beta \sin \theta \tag{47}$$

Substituting Equation (47) into Equation (2) gives:

$$\begin{aligned} \Delta u &= \psi_f \omega \sin \hat{\theta} \cos \theta - \psi_f \omega \cos \hat{\theta} \sin \theta \\ &= -\psi_f \omega \sin(\theta - \hat{\theta}) \end{aligned} \tag{48}$$

When the PI controller adjusts Δu to $\theta = \hat{\theta}$, it becomes possible to calculate the estimated position of the rotor [27]. The process of parameterizing K_p and K_i in the PI controller is as follows:

When $\theta - \hat{\theta}$ is approximately equal to 0, the PLL structure diagram shown in Figure 3 can be simplified to Figure 4.

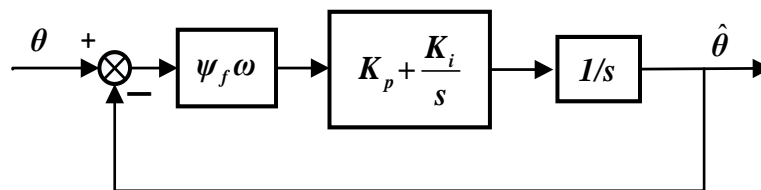


Figure 4. Phase-locked loop equivalent structure.

In Figure 4, the open-loop transfer function is:

$$G(s) = \psi_f G(K_p + \frac{K_i}{s}) \frac{1}{s} = \frac{\psi_f \omega (K_p s + K_i)}{s^2} \tag{49}$$

The closed-loop transfer function is:

$$\Phi(s) = \frac{\psi_f \omega K_p s + \psi_f \omega K_i}{s^2 + \psi_f \omega K_p s + \psi_f \omega K_i} \tag{50}$$

The typical form of a second-order system is determined by taking this as the tuning parameter.

$$G(s) = \frac{\omega_n^2}{s^2 + 2\zeta\omega_n s + \omega_n^2} \tag{51}$$

The closed-loop transfer function can be calculated using the standard form of a second-order system, resulting in the following equation.

$$\begin{cases} \psi_f \omega K_p = 2\zeta\omega_n \\ \psi_f \omega K_i = \omega_n^2 \end{cases} \tag{52}$$

K_p and K_i can be calculated from Equation (52).

4.2. Design of Adaptive Quadrature Phase-Locked Loop

In the control system depicted in Figure 2, the counter-potential obtained through estimation by a discrete variable gain sliding mode observer is fed into the quadrature phase-locked loop (QPLL) for rotor position calculation [28]. Compared to a basic phase-locked loop with a fixed bandwidth, the adaptive quadrature phase-locked loop can dynamically adjust its bandwidth based on the rotational speed of the motor [29]. This adjustment effectively reduces estimation errors in the rotor position and enhances accuracy in rotor position estimation, thereby enabling proper decoupling of rotor current and resulting in higher torque output [30]. As illustrated in Figure 5, when feeding estimated anti-potential information into the adaptive quadrature phase-locked loop, an adaptive filter needs to be incorporated to eliminate harmonic components present in the anti-potential information. The transfer function of this quadrature phase-locked loop is as follows:

$$G_{PLL}(s) = \frac{\hat{e}k_p s + \hat{e}k_i}{s^2 + \hat{e}k_p s + \hat{e}k_i} \tag{53}$$

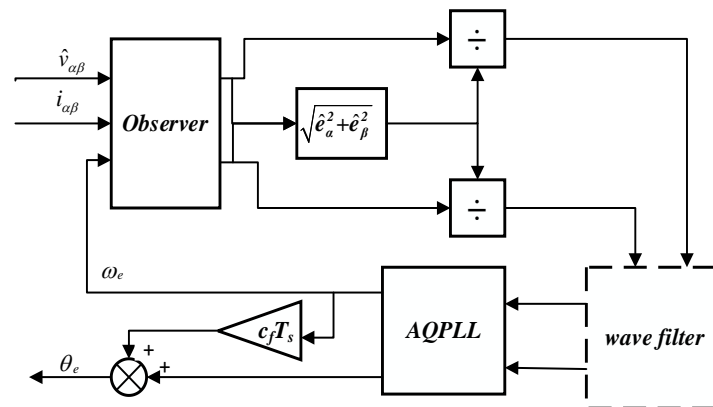


Figure 5. Position velocity estimation strategy.

In order to reduce the error of the back EMF, the back EMF can be normalized by Equation (54).

$$\hat{e} = \hat{e} / \sqrt{\hat{e}_\alpha^2 + \hat{e}_\beta^2} \tag{54}$$

After normalizing the inverse potential, the bandwidth of the quadrature phase-locked loop is no longer affected by the rotor speed [31]. As a result, the transfer function can be simplified as:

$$G_{PLL}(s) = \frac{k_p s + k_i}{s^2 + k_p s + k_i} \tag{55}$$

We can replace the poles in Equation (55) with Equation (56) as follows:

$$\begin{aligned} k_p(h) &= 2\tau\rho(h) \\ k_i(h) &= \rho^2(h) \end{aligned} \tag{56}$$

where τ is the damping coefficient; ρ is the AQPLL tuning parameter; h is the discrete time step parameter.

Because it is difficult to adjust both τ and ρ at the same time and the bandwidth of the QPLL is related to ρ , the damping coefficient is set to a constant value in order to simplify the calculation process. The AQPLL tuning parameter ρ is set as follows:

$$\rho(h) = \rho(h - 1) - \mu \frac{1}{2} \left(\frac{\partial \varepsilon_e(h)}{\partial h(h - 1)} \right) \tag{57}$$

where μ is the step parameter of the adaptive speed and ε_e is the PI controller input error of the QPLL.

The final equation for updating the tuning parameters can be expressed as:

$$\rho(h) = \rho(h - 1) - \mu z_1(h)z_2(h) = \rho(h - 1) - \Delta\rho(h) \tag{58}$$

where z_1 and z_2 parameters are set as follows:

$$\begin{aligned} z_1(h) &= \hat{e}_{\alpha n}^f(h) \sin(\hat{\theta}_e(h - 1)) - \hat{e}_{\beta n}^f(h) \cos(\hat{\theta}_e(h - 1)) \\ z_2(h) &= 2\tau\varepsilon_e(h - 1) + T_s p(h - 1)(\varepsilon_e(h - 1) - \varepsilon_e(h - 2)) \end{aligned} \tag{59}$$

where $[\hat{e}_{\alpha n}^f, \hat{e}_{\beta n}^f]$ is the filtered counter-potential estimate.

The AQPLL logic block diagram designed based on the above analysis is shown in Figure 6.

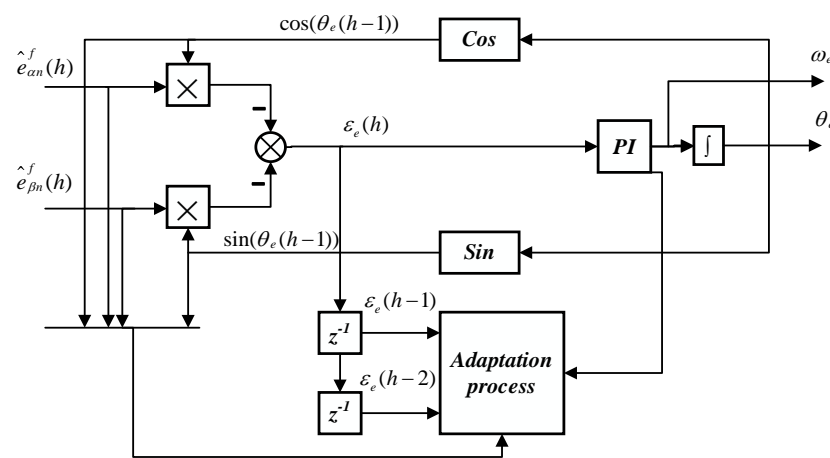


Figure 6. AQPLL framework diagram.

4.3. Stability Analysis

To analyze the stability of AQPLL as ρ varies, we use Equation (56) in Equation (55) to calculate the root of the AQPLL characteristic equation.

$$s_{1,2} = -\tau\rho \pm \rho\sqrt{(\tau^2 - 1)} \tag{60}$$

According to the literature [32], the roots of the characteristic equation remain in the left half-s plane as long as $\rho > 0$, indicating stability of the AQPLL system. It is difficult to observe the counter-potential accurately when the motor is running at lower speeds, so it is necessary to limit the minimum speed of the motor, i.e., the value of ρ :

$$\rho \geq \rho_{\min} \tag{61}$$

where ρ_{\min} is the minimum value of ρ that can lock the motor frequency during motor startup.

The computation of the observer gain is only possible if the observer’s dynamic response is faster than the PMSM state change. Additionally, the observer gain is limited by the observer state feedback [33].

$$\dot{\hat{x}}_{\alpha\beta} = (A(\hat{\omega}_e) - KC)\hat{x}_{\alpha\beta} + Bv_{\alpha\beta}^* + \tilde{K}i_{\alpha\beta} \tag{62}$$

where the matrix expression for C is $\begin{bmatrix} 1 & 0 & 0 & 0 \\ 0 & 1 & 0 & 0 \end{bmatrix}$; $\hat{x}_{\alpha\beta}$ is the observer gain.

Note that the observer gain in Equation (62) must be valid for the entire speed range of the motor and the closed-loop poles must remain in the left half-s plane [34].

5. Simulation Experiments

In order to verify the effectiveness of the proposed method, fixed gain and variable gain super-torsional sliding mode observers were constructed in MATLAB/Simulink, as shown in Figure 2. The adaptive orthogonal phase-locked loop (PLL) method is used to obtain the rotor position of both observers, and a PI controller is used in the speed loop of the motor control system. Simulation experiment parameters are shown in the following table. The horizontal coordinate in the figure below represents the time used in the simulation, and the vertical coordinate represents the rotor speed comparison, rotor speed error, rotor position comparison, and rotor position error.

Table 1 includes the values of the parameters used in the experiment: R_s represents the stator resistance of the motor; V_{DC} indicates the voltage level of the motor; L_s denotes the stator inductance; ω_{rmax} signifies the maximum allowable speed of the motor; power refers to the power supply's output. T_s represents the sampling period. $K_{\eta 1}$, $K_{\eta 2}$, and K_v are constants; ω_c is defined as the cut-off frequency; λ_{pm} represents a permanent magnet flux linkage; J stands for moment of inertia; pole pairs indicate the number of poles present in the motor structure; B represents magnetic induction intensity. ω_r denotes motor speed, while ω_f signifies the filter cut-off frequency. Q is used to represent the quality factor.

Table 1. Simulation platform parameters.

Parameter	Value	Parameter	Value
R_s	2.875 Ω	λ_{pm}	0.175 Wb
T_s	0.1 ms	J	0.85 mKgm ²
L_s	85 mH	B	0.373 mNm/s
$K_{\eta 1}$	0.3861	$K_{\eta 2}$	750
ω_{rmax}	3000 rpm	ω_f	$2\pi 10$ rad/s
K_v	0.999	Tioad(ω_r)	(0.00142 ω_r) Nm
V_{DC}	300 V	Pole Pairs	4
Power	100 W	Q	50

Figure 7 shows the actual versus estimated speed waveforms of the output of the fixed gain super-twisting sliding mode observer for an initial speed of 500 r/min at no load on the motor, 1000 r/min given at 0.1 s, and 2500 r/min at 0.2 s. The output of the fixed gain super-twisting sliding mode observer is shown in Figure 8, which shows the actual versus estimated speed waveforms.

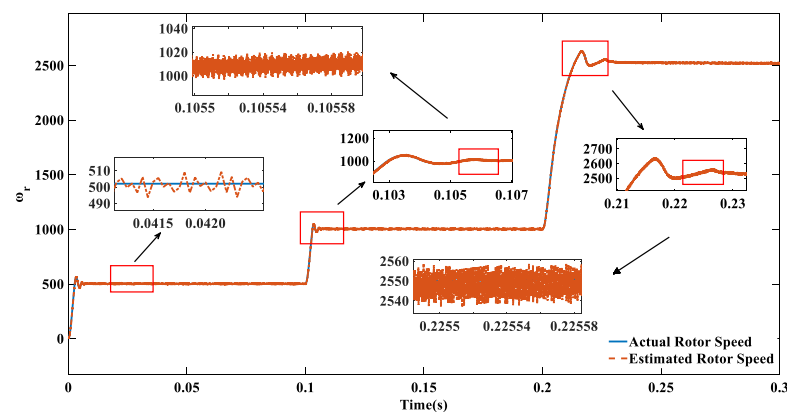


Figure 7. Fixed gain STA-SMO estimated speed vs. actual speed.

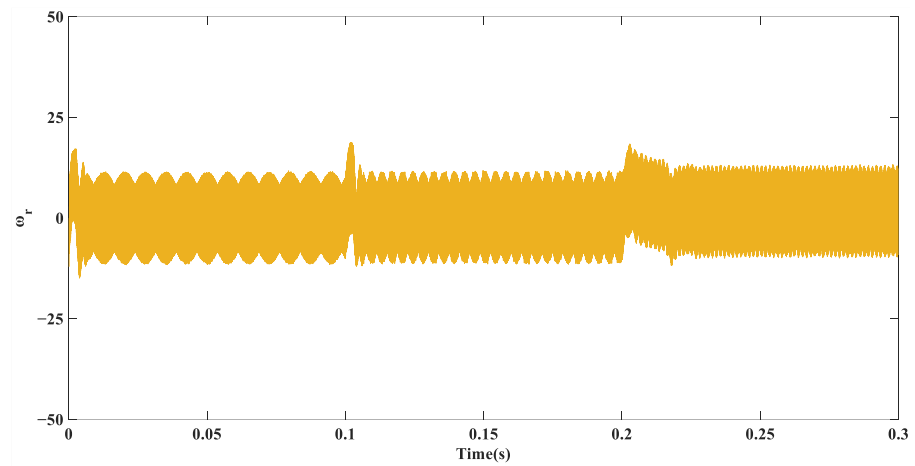


Figure 8. Fixed gain STA-SMO speed error.

Figures 7 and 8 show that when fixed gain STA-SMO is used, the speed error remains around 10 r/min because the fixed gain sliding mode parameter is calculated based on the maximum and minimum speed of the rotor, so the speed error does not fluctuate much when the speed varies.

Figures 9 and 10 show the estimated rotor position and the actual rotor position information when the fixed gain sliding mode observer is used. From the figure, it can be seen that the rotor position error increases as the motor speed increases.

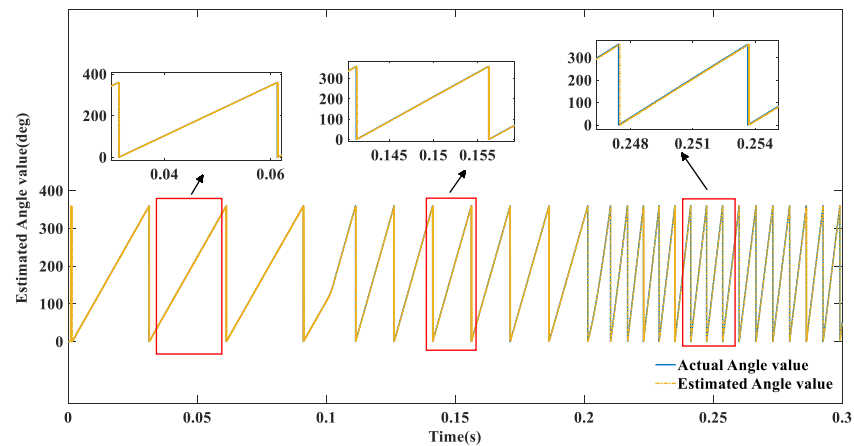


Figure 9. Fixed gain STA-SMO actual vs. estimated positions.

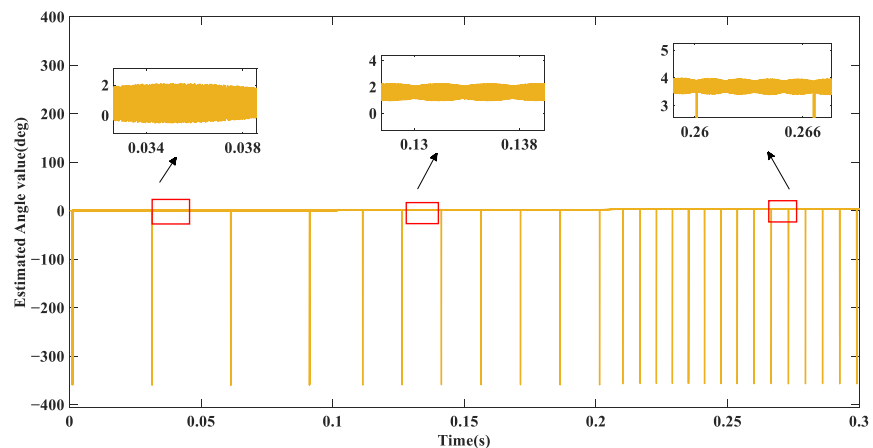


Figure 10. Fixed gain STA-SMO rotor position error.

The actual speed exhibits a slight decrease relative to the reference speed when different loads are added at 0.15 s and 0.25 s, as depicted in Figure 11 and Figure 12, respectively; however, the error between the estimated speed and the actual speed remains constant at 10 r/min.

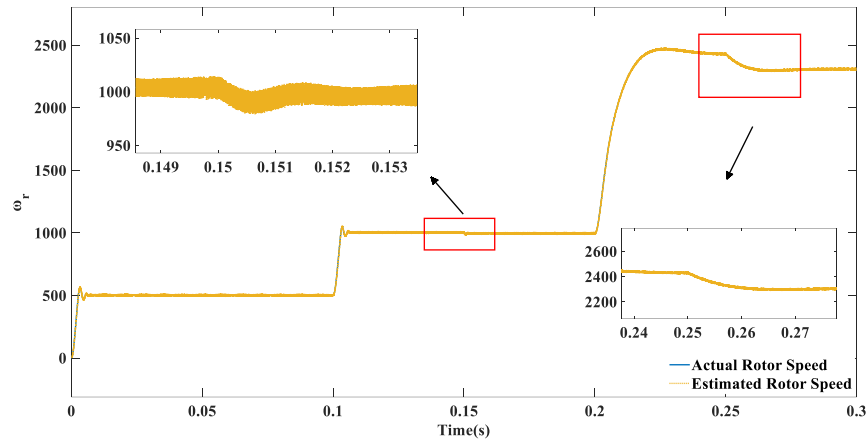


Figure 11. Estimated vs. actual speed with load for fixed gain STA-SMO.

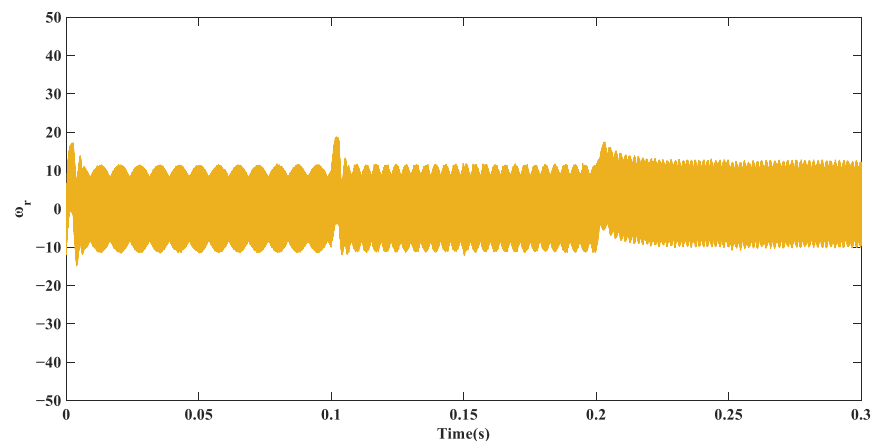


Figure 12. Speed error with load for fixed gain STA-SMO.

The waveforms of the estimated rotor position and the actual rotor position with loads, along with their corresponding position errors, are depicted in Figures 13 and 14. The obtained results indicate that under different load conditions, when estimating the rotor position using a fixed gain approach, the position error is approximately 2 radians at 0.15 s and around 4 radians at 0.25 s.

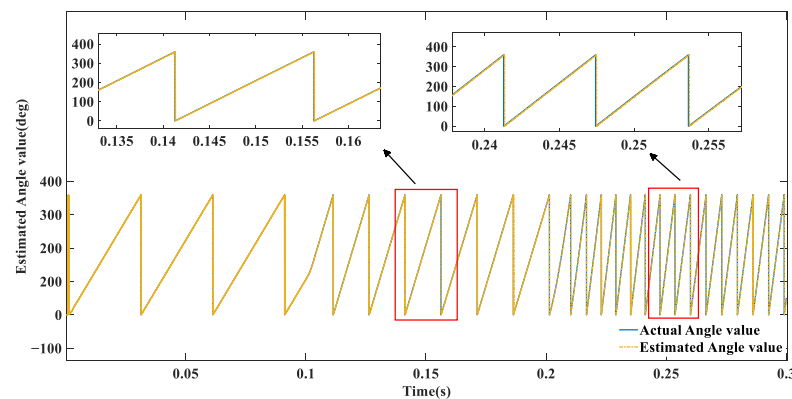


Figure 13. Actual vs. estimated position of fixed gain STA-SMO with loads.

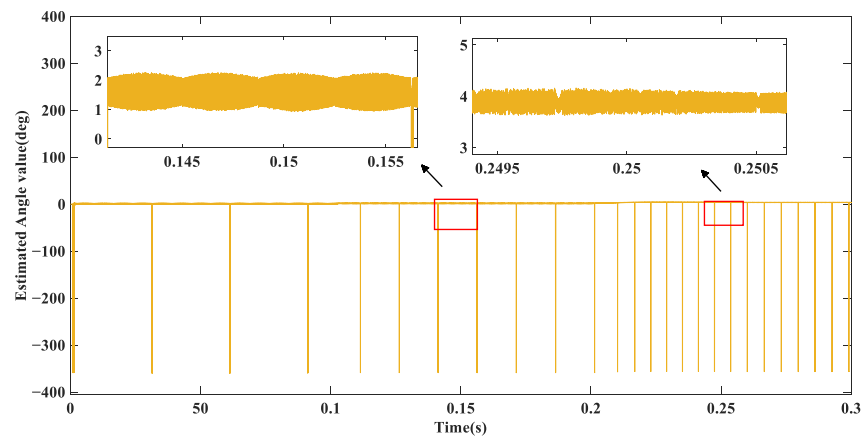


Figure 14. Position error with load for fixed gain STA-SMO.

Figures 15 and 16 show the motor speed and the actual speed information estimated using the variable gain super-twisting sliding mode observer for a given speed variation when the motor is unloaded.

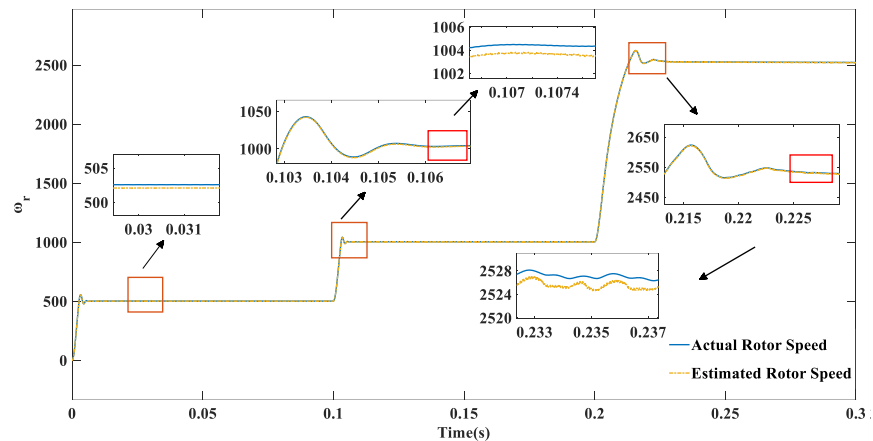


Figure 15. Variable gain STA-SMO estimation vs. actual rotational velocity.

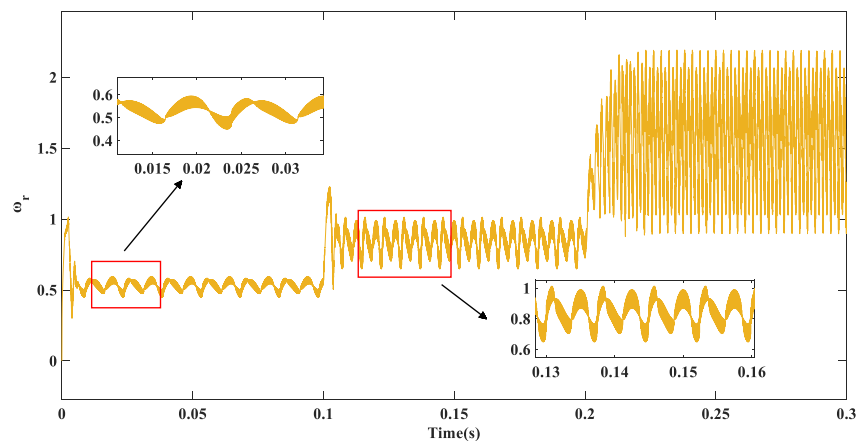


Figure 16. Variable gain STA-SMO speed error.

As shown in Figure 15, the variable gain super-twisting sliding mode observer not only eliminates the high-frequency jittering observed in Figure 7, but also results in improved convergence of the estimates to the true values. As can be seen from the enlarged view of Figure 16, the maximum error is only 0.6 r/min when the given speed is 500 r/min. When

the 0.1 s speed is 1000 r/min, the speed error is only 1 r/min. And when the motor is in the high-speed domain at 2500 r/min, the speed error is only 2 r/min.

From Figures 17 and 18, it can be seen that the rotor position error is always kept small when the rotational speed is at 500 r/min, 1000 r/min, and 2500 r/min, respectively.

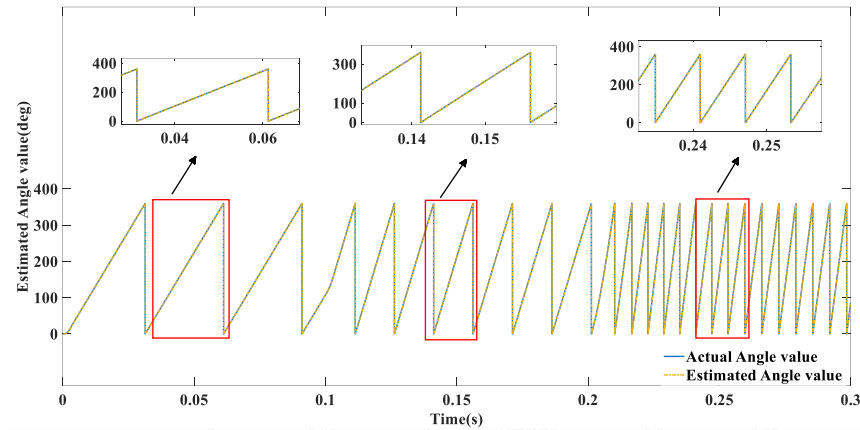


Figure 17. Variable gain STA-SMO actual position vs. estimated position.

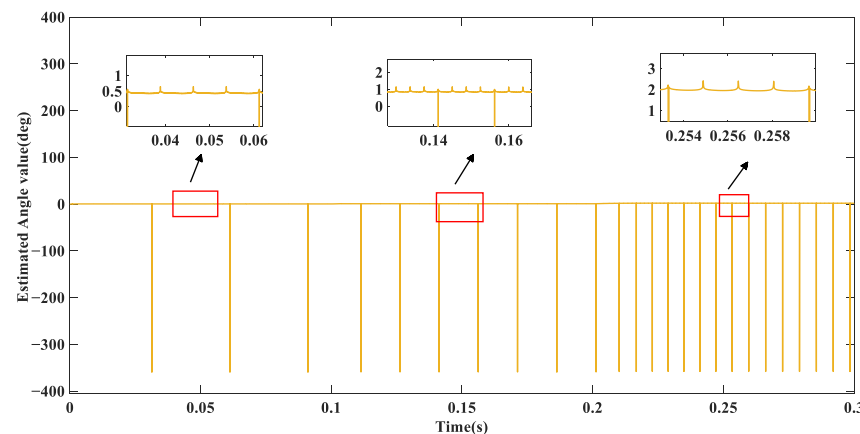


Figure 18. Variable gain STA-SMO estimation vs. actual rotor position error.

From the comparison between Figures 10 and 18, it can be seen that the rotor position estimation accuracy is higher and the position estimation error is reduced by half when the variable gain super-twisting sliding mode observer is used.

To verify the stability of the variable gain super-twisting sliding mode observer with load, a load of 4 N-M was added at 0.15 s and raised to 10 N-M at 0.25 s. The rotational speed and positional errors were observed for a given constant rotational speed.

From Figure 19, it can be seen that the estimated and actual speed decreases by 10 r/min when the load is applied suddenly at 0.15 s and stabilizes to 998 r/min at 0.152 s. Likewise, when the load is abruptly increased at 0.25 s, the speed will decrease by 150 revolutions per minute and will stabilize after 0.01 s. From Figures 20 and 21 it can be seen that sudden loading has no effect on the speed error and rotor position error, which also shows the observation accuracy of this observer with a load.

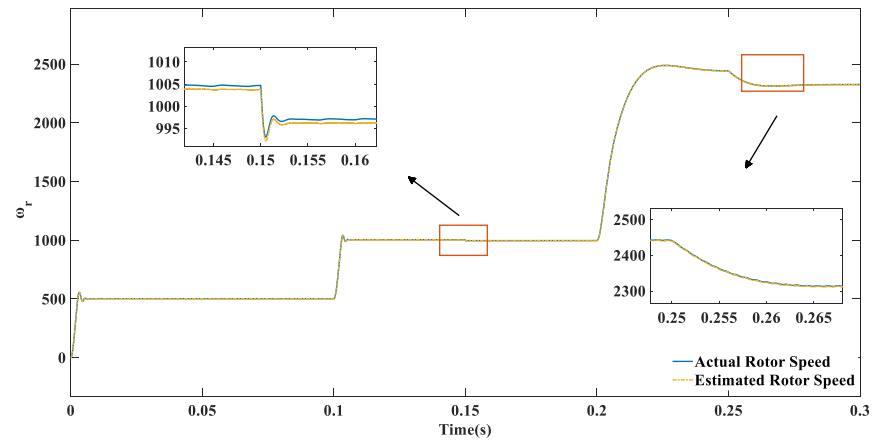


Figure 19. Estimated vs. actual speed with loads for variable gain STA-SMO.

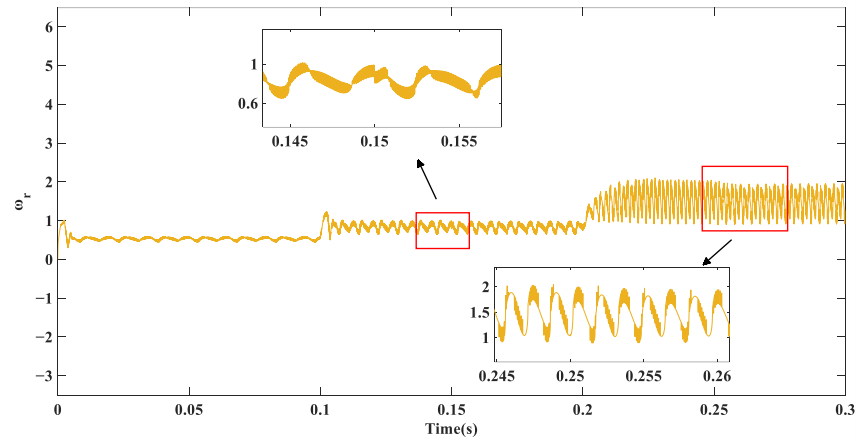


Figure 20. Speed error with loads for variable gain STA-SMO.

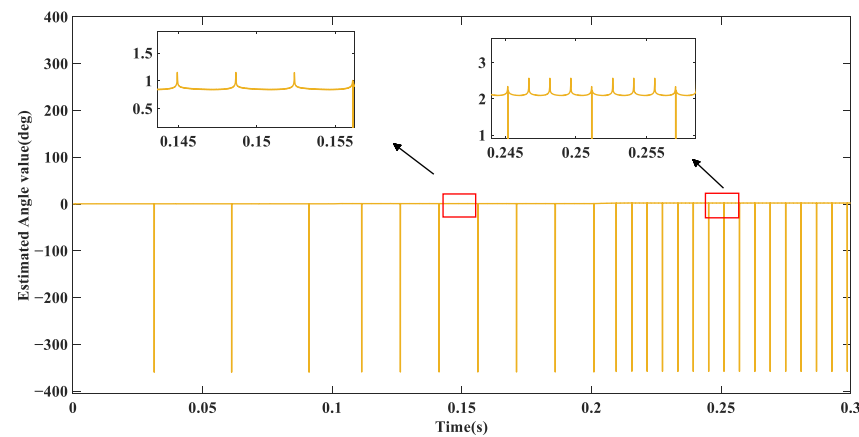


Figure 21. Position error with loads for variable gain STA-SMO.

Figures 20 and 22 Everyone has agreed demonstrate the performance of the variable gain STA-SMO under loads. The variable gain module reacts quickly to sudden load additions at 0.15 s and 0.25 s by adjusting the sliding mode control rate in real-time based on the rotor speed change. The simulation results show that the variable gain STA-SMO can accurately estimate the rotor speed and position under various operating conditions of the motor.

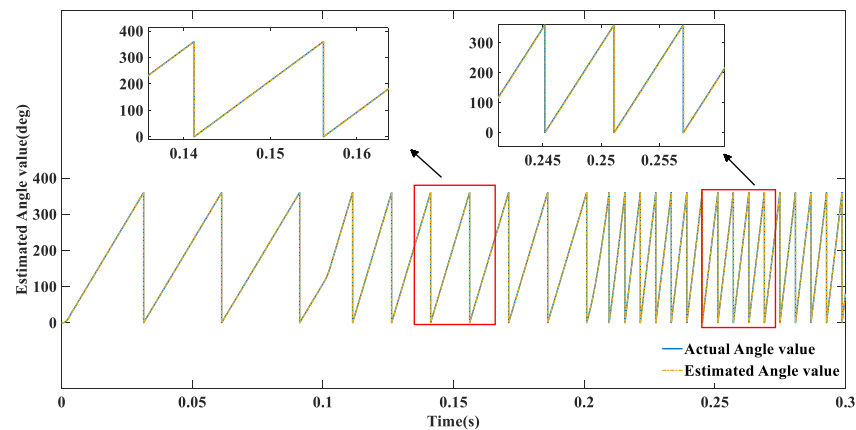


Figure 22. Actual vs. estimated position of variable gain STA-SMO with loads.

6. Conclusions

A sensor-less estimation method of a permanent magnet synchronous motor based on a discrete variable gain super-twisting sliding mode observer and adaptive orthogonal phase-locked loop is proposed. The signal estimated by the discrete variable gain super-twisting sliding mode observer can effectively avoid buffering, and can quickly track the rotor speed and position in real time, so as to minimize the error between the actual value and the estimated value. The parameters in the adaptive orthogonal PLL can also be adjusted according to the motion state of the rotor, which effectively improves the problem of the poor tracking performance of the rotor caused by the fixed bandwidth in the traditional PLL. The simulation results show that the speed error of the fixed gain observer is about 10 r/min when the speed is 500 r/min, 1000 r/min and 2500 r/min, while the speed error of the variable gain observer is only 1 r/min. Therefore, the performance of the variable gain observer in rotor speed estimation is better than that of the fixed gain observer. In terms of rotor position estimation, the rotor position error shown by the variable gain observer is only half that of the fixed gain observer. Moreover, when the system speed is switched, the response time required by the variable gain observer is shorter and closer to the actual situation. In order to further study the observation of the proposed estimation method under loads, different loads were added at 0.15 s and 0.25 s, respectively. The simulation results show that under the influence of a load, the estimated performance of rotor speed and position is not weakened, and the error between the estimated value and the actual value is the same as that when the load is 0, so the rotor position can be controlled with high precision.

Author Contributions: Algorithm design, M.L.; coding and testing, M.L; mathematical derivation, M.L. and Y.Z.; article review and proofreading, X.L.; funding acquisition, X.L. and F.X. All authors have read and agreed to the published version of the manuscript.

Funding: This work was supported by the Science and Technology Major Project of Inner Mongolia Autonomous Region (2020ZD0014).

Institutional Review Board Statement: Not applicable.

Informed Consent Statement: Not applicable.

Data Availability Statement: The original contributions presented in the study are included in the article, further inquiries can be directed to the corresponding author.

Acknowledgments: We would like to acknowledge the School of Rail Transportation of Shandong Jiaotong University for providing the experimental equipment and assistance with the experimental testing.

Conflicts of Interest: The authors declare no conflicts of interest.

References

1. Yu, B.; Shen, A.; Chen, B.; Luo, X.; Tang, Q.; Xu, J.; Zhu, M. A compensation strategy of flux linkage observer in SPMSM sensor-less drives based on linear extended state observer. *IEEE Trans. Energy Convers.* **2021**, *37*, 824–831. [\[CrossRef\]](#)
2. Yang, Y. *Research on Position Sensor-Less Control System of Permanent Magnet Synchronous Motor*; Harbin Institute of Technology: Harbin, China, 2018.
3. Shen, Y.; Liu, A.; Cui, G.; Yang, X.; Zheng, Z. Sensor-less vector control of permanent magnet synchronous motor with extended sliding mode observer. *J. Electr. Mach. Control.* **2020**, *24*, 8. [\[CrossRef\]](#)
4. Volpato Filho, C.J.; Xiao, D.; Vieira, R.P.; Emadi, A. Observers for high-speed sensor-less pmsm drives: Design methods, tuning challenges and future trends. *IEEE Access* **2021**, *9*, 56397–56415. [\[CrossRef\]](#)
5. Wu, Z.; Li, R. Sensor-less control of PMSM based on sliding mode variable structure control and adaptive sliding mode observer. In Proceedings of the 2021 24th International Conference on Electrical Machines and Systems (ICEMS), Gyeongju, Republic of Korea, 31 October–3 November 2021; pp. 2015–2019.
6. Zribi, M.; Chiasson, J. Position control of a PM stepper motor by exact linearization. *IEEE Trans. Autom. Control* **1991**, *36*, 620–625. [\[CrossRef\]](#)
7. Yao, Y.; Huang, Y.; Peng, F.; Dong, J.; Zhu, Z. Compensation method of position estimation error for high-speed surface-mounted PMSM drives based on robust inductance estimation. *IEEE Trans. Power Electron.* **2021**, *37*, 2033–2044. [\[CrossRef\]](#)
8. Tang, Q.; Yu, B.; Luo, P.; Luo, X.; Shen, A.; Xia, Y.; Xu, J. Second Harmonic Seamless Splicing Technique Based on Maximum Active-Voltage Vector for Online MTPA Tracking Control of SynRM. *IEEE Trans. Ind. Electron.* **2021**, *69*, 10958–10968. [\[CrossRef\]](#)
9. Luo, X.; Shen, A.; Tang, Q.; Liu, J.; Xu, J. Two-step continuous-control set model predictive current control strategy for SPMSM sensor-less drives. *IEEE Trans. Energy Convers.* **2020**, *36*, 1110–1120. [\[CrossRef\]](#)
10. Ding, S.; Hou, Q.; Wang, H. Disturbance-observer-based second-order sliding mode controller for speed control of PMSM drives. *IEEE Trans. Energy Convers.* **2022**, *38*, 100–110. [\[CrossRef\]](#)
11. Wang, M.; Sun, D.; Zheng, Z.; Nian, H. A novel lookup table based direct torque control for OW-PMSM drives. *IEEE Trans. Ind. Electron.* **2020**, *68*, 10316–10320. [\[CrossRef\]](#)
12. Xiong, Y.; Wang, A.; Zhang, T. Sensor-Less Complex System Control of PMSM Based on Improved SMO. In Proceedings of the 2021 6th International Conference on Automation, Control and Robotics Engineering (CACRE), Dalian, China, 15–17 July 2021; pp. 228–232.
13. Guo, L.; Wang, H.; Jin, N.; Dai, L.; Cao, L.; Luo, K. A speed sensor-less control method for permanent magnet synchronous motor based on super-twisting sliding mode observer. In Proceedings of the 2019 14th IEEE Conference on Industrial Electronics and Applications (ICIEA), Xi'an, China, 19–21 June 2019; pp. 1179–1184.
14. Zhang, J.; Tian, J.; Alcaide, A.M.; Leon, J.I.; Vazquez, S.; Franquelo, L.G.; Luo, H.; Yin, S. Lifetime Extension Approach Based on Levenberg-Marquardt Neural Network and Power Routing of DC-DC Converters. *IEEE Trans. Power Electron.* **2023**, *38*, 10280–10291. [\[CrossRef\]](#)
15. Ke, W.; Sun, D.; Zhang, X.; Nian, H.; Hu, B. Adaptive Capacitor Voltage-Based Model Predictive Control for Open-Winding PMSM System with a Floating Capacitor. *IEEE J. Emerg. Sel. Top. Power Electron.* **2022**, *11*, 442–452. [\[CrossRef\]](#)
16. Sun, C.; Sun, D.; Chen, W.; Nian, H. Improved model predictive control with new cost function for hybrid-inverter open-winding PMSM system based on energy storage model. *IEEE Trans. Power Electron.* **2021**, *36*, 10705–10715. [\[CrossRef\]](#)
17. Chen, W.; Sun, D.; Wang, M.; Nian, H. Modeling and control for open-winding PMSM under open-phase fault based on new coordinate transformations. *IEEE Trans. Power Electron.* **2020**, *36*, 6892–6902. [\[CrossRef\]](#)
18. Wang, M.; Sun, D.; Ke, W.; Nian, H. A universal lookup table-based direct torque control for OW-PMSM drives. *IEEE Trans. Power Electron.* **2020**, *36*, 6188–6191. [\[CrossRef\]](#)
19. Sun, D.; Chen, W.; Cheng, Y.; Nian, H. Improved direct torque control for open-winding PMSM system considering zero-sequence current suppression with low switching frequency. *IEEE Trans. Power Electron.* **2020**, *36*, 4440–4451. [\[CrossRef\]](#)
20. Zheng, Z.; Sun, D.; Wang, M.; Nian, H. A dual two-vector-based model predictive flux control with field-weakening operation for OW-PMSM drives. *IEEE Trans. Power Electron.* **2020**, *36*, 2191–2200. [\[CrossRef\]](#)
21. Hu, W.; Ruan, C.; Nian, H.; Sun, D. An improved modulation technique with minimum switching actions within one PWM cycle for open-end winding PMSM system with isolated DC bus. *IEEE Trans. Ind. Electron.* **2019**, *67*, 4259–4264. [\[CrossRef\]](#)
22. Cheng, Y.; Sun, D.; Chen, W.; Nian, H. Model predictive current control for an open-winding PMSM system with a common DC bus in 3-D space. *IEEE Trans. Power Electron.* **2020**, *35*, 9597–9607. [\[CrossRef\]](#)
23. Zheng, Z.; Sun, D.; Wang, M.; Nian, H. Model predictive control with a novel cost function evaluation scheme for OW-PMSM drives. *Electron. Lett.* **2020**, *56*, 655–657. [\[CrossRef\]](#)
24. Zheng, Z.; Sun, D. Model predictive flux control with cost function-based field weakening strategy for permanent magnet synchronous motor. *IEEE Trans. Power Electron.* **2019**, *35*, 2151–2159. [\[CrossRef\]](#)
25. Zhou, Q.; Wang, Y.; Shi, K.; Zhang, F.; Du, H. High-frequency pulsating voltage injection PMSM position sensor-less control based on generalized second-order integrator. *J. Electr. Mach. Control* **2023**, 1–10.
26. Chen, B. *Research on Medium and High Speed Control Technology and Starting Strategy of Permanent Magnet Synchronous Motor without Position Sensor*; Huazhong University of Science and Technology: Wuhan, China, 2021.
27. Liu, G.; Zhang, H.; Song, X. Position-estimation deviation-suppression technology of PMSM combining phase self-compensation SMO and feed-forward PLL. *IEEE J. Emerg. Sel. Top. Power Electron.* **2020**, *9*, 335–344. [\[CrossRef\]](#)

28. Chen, S. *Research on Position Sensor-Less Control Strategy of Permanent Magnet Synchronous Motor in Full Speed Domain*; China University of Mining and Technology: Beijing, China, 2020.
29. Lascu, C.; Andreescu, G.D. PLL position and speed observer with integrated current observer for sensor-less PMSM drives. *IEEE Trans. Ind. Electron.* **2020**, *67*, 5990–5999. [[CrossRef](#)]
30. Tang, Q.; Chen, D.; He, X. Integration of improved flux linkage observer and I-f starting method for wide-speed-range sensorless SPMSM drives. *IEEE Trans. Power Electr.* **2019**, *35*, 8374–8383. [[CrossRef](#)]
31. Chen, D.; Liu, X.; Yu, W.; Zhu, L.; Tang, Q. Neural-network based adaptive self-triggered consensus of nonlinear multi-agent systems with sensor saturation. *IEEE Trans. Netw. Sci. Eng.* **2021**, *8*, 1531–1541. [[CrossRef](#)]
32. Hu, W.; Ruan, C.; Nian, H.; Sun, D. Zero-sequence current suppression strategy with common-mode voltage control for open-end winding PMSM drives with common DC bus. *IEEE Trans. Ind. Electron.* **2020**, *68*, 4691–4702. [[CrossRef](#)]
33. Novak, Z.; Novak, M. Adaptive PLL-based sensor-less control for improved dynamics of high-speed PMSM. *IEEE Trans. Power Electron.* **2022**, *37*, 10154–10165. [[CrossRef](#)]
34. Wang, H.; Yang, Y.; Ge, X.; Zuo, Y.; Yue, Y.; Li, S. PLL-and FLL-based speed estimation schemes for speed-sensor-less control of induction motor drives: Review and new attempts. *IEEE Trans. Power Electron.* **2021**, *37*, 3334–3356. [[CrossRef](#)]

Disclaimer/Publisher’s Note: The statements, opinions and data contained in all publications are solely those of the individual author(s) and contributor(s) and not of MDPI and/or the editor(s). MDPI and/or the editor(s) disclaim responsibility for any injury to people or property resulting from any ideas, methods, instructions or products referred to in the content.